ADVANCED ENGINEERING MATERIALS
www.aem-journal.com

A Perspective on Powder Metallurgy and Additive Manufacturing of High-Nitrogen Alloyed Stainless Steels

Louis Becker, Felix Radtke, Jonathan Lentz, Simone Herzog, Christoph Broeckmann, and Sebastian Weber*

Incorporating nitrogen as an alloying element in stainless steels can significantly enhance their mechanical and chemical properties. However, the limited solubility of nitrogen, particularly in the liquid phase, presents challenges. This perspective article explores an innovative powder metallurgical approach to producing high-nitrogen steels (HNS) by utilizing a mixture of stainless steel and Si_3N_4. This mixture undergoes hot isostatic pressing (HIP) followed by direct quenching, facilitating diffusion alloying, and solution annealing in a single step. The article also examines adapting this method to powder bed fusion of metals using a laser beam (PBF-LB/M) to overcome nitrogen solubility limits, which currently constrain the achievable nitrogen content in PBF-LB/M-manufactured stainless steels. The approach aims to retain Si_3N_4 particles within the matrix during PBF-LB/M to enrich the steel with nitrogen during subsequent HIP. However, laser interaction with Si_3N_4 can lead to nitrogen loss, prompting an alternative strategy: a shell–core structure based on a gas-tight shell enclosing loose Si_3N_4 particles. These particles dissolve during HIP, enriching the matrix with nitrogen and enabling the production of HNS. This article highlights the potential for extending this approach to other stainless steel groups, broadening the possibilities for HNS production through both conventional HIP and PBF-LB/M manufacturing routes.

Preface

This article presents results from the project "Influence of an Si_3N_4 powder additive on the PBF-LB processability of stainless steels and the microstructure development during PBF-LB and subsequent HIP-URQ redensification," which is funded by the German Research Foundation within the framework of the SPP 2122 called "Materials for Additive Manufacturing (MATframe)." It is intended to provide a comprehensive insight into the results by placing already published results in an overall context with results that have not yet been published. The results and discussion of those investigations that have not yet been published and are presented for the first time in this article are preceded by a brief motivation and an experimental section. The motivation is embedded in the overall context of the article.

L. Becker, J. Lentz, S. Weber
Chair of Materials Technology
Ruhr University Bochum
44801 Bochum, Germany
E-mail: Louis.Becker@rub.de

F. Radtke, S. Herzog, C. Broeckmann
Institute of Applied Powder Metallurgy and Ceramics
RWTH Aachen e. V.
52062 Aachen, Germany

The ORCID identification number(s) for the author(s) of this article can be found under https://doi.org/10.1002/adem.202402033.

DOI: 10.1002/adem.202402033

1. Introduction

1.1. General Aspects About Stainless Steels

Stainless steels, characterized by their high chromium content, are known for their resistance to corrosion and oxidation in various environments. Originally developed for cutlery and household applications, stainless steels have become indispensable materials in industries as diverse as aerospace, marine, automotive, construction, energy, and healthcare.[1–3] The corrosion resistance of stainless steels is based on the formation of a Cr-rich oxide layer resulting from the addition of at least 10.5 mass% chromium.[3–5] The tightly adhering and dense passive layer, which is only a few nanometers thick, inhibits the anodic metal dissolution of the steel due to its low ionic conductivity and can heal local damage under favorable environmental conditions (repassivation).[3] However, the presence of the passive layer entails the risk of localized corrosion phenomena such as pitting corrosion, which occurs due to either mechanical or chemical damage to the passive layer, resulting in the formation of holes or cavities that propagate from the surface into the metal's interior.[3,6] The resistance of stainless steels to pitting corrosion is influenced by alloy additions and can be evaluated by the pitting resistance equivalent number (PREN), calculated according to Equation (1)[3]

$$\mathrm{PREN} = [\%\mathrm{Cr}] + 3.3\,[\%\mathrm{Mo}] + a\,[\%\mathrm{N}] \tag{1}$$

where a ranges from 13 to 30. The measure of alloying for resistance to corrosion (MARC) is an actualized formula that has been extended to account for the negative effects of manganese

and nickel on corrosion resistance while also accounting for a previously reported effect of carbon that increases corrosion resistance[7]

$$\begin{aligned}\mathrm{MARC} = {} & [\%\mathrm{Cr}] + 3.3\,[\%\mathrm{Mo}] + 20\,[\%\mathrm{C}] + 20\,[\%\mathrm{N}] \\ & - 0.5\,[\%\mathrm{Mn}] - 0.25\,[\%\mathrm{Ni}]\end{aligned} \tag{2}$$

The elements from the two shown formulas provide a good overview of the alloying elements found in stainless steels. These elements not only influence the resistance to pitting, but also significantly determine the phase constitution of a stainless steel. Nickel, manganese, carbon, and nitrogen are known to stabilize the austenitic phase, that is, the face-centered-cubic (fcc) lattice, while chromium and molybdenum lead to the stabilization of the ferritic phase, which has a body-centered-cubic (bcc) lattice.[3,8] Depending on their chemical composition and thus the proportion of austenitic and ferritic stabilizing elements, stainless steels can be divided into austenitic, ferritic, austenitic–ferritic (duplex), and martensitic stainless steels.[3]

1.2. Ferritic Stainless Steels

The basic alloy composition of ferritic stainless steels is based on the FeCr system. X6Cr13 is the most economical variant, which can be alloyed with increased chromium content, such as X6Cr17, to improve corrosion resistance.[3] Other alloying elements commonly alloyed into ferritic steels include titanium, which is used to bind carbon and increase resistance to intergranular corrosion; molybdenum, which increases resistance to pitting; and niobium, which is used either as a carbon binder or to increase strength through the formation of Laves phase, particularly in high-temperature applications.[3,9] The bcc lattice of ferritic stainless steels, due to its higher diffusion rates compared to the closely packed fcc lattice, predisposes these steels to the formation of coarse grains, which adversely affects ductility and transition temperature.[10] As a result, small amounts of austenite-stabilizing elements such as manganese and nickel can be alloyed to achieve a fractional austenitic phase and mitigate grain growth during thermal processing.[3] An inherent advantage of the bcc lattice is its reduced coefficient of thermal expansion compared to the fcc lattice, resulting in superior thermal cycling performance.[11]

1.3. Austenitic Stainless Steels

Austenitic stainless steels are primarily composed of the FeCrNi system, with the addition of manganese and nitrogen to strengthen the austenitic phase stability.[3,12] The typical representative, X6CrNi18-8 (DIN EN 1.4308, AISI 304) stainless steel, which contains 18 mass% chromium and 8 mass% nickel, is an example of the standard alloy in this category.[12] Enhanced grades, such as X5CrNiMo17-12-2 (DIN EN 1.4401, AISI 316) stainless steel, contain up to 3 mass% molybdenum to significantly improve resistance to chloride-induced pitting and crevice corrosion.[3] The austenitic structure is preferred for its high toughness and ductility over a wide range of temperatures due to its fcc lattice, which is inherently more ductile and capable of significant work hardening compared to the bcc lattice.[3,12] In addition to FeCrNi austenites, there are also FeCrMn austenites, which contain elevated levels of nitrogen or a combination of nitrogen and carbon. These alloys not only exhibit higher strength due to significant solid solution strengthening but also serve as a more cost-effective alternative to FeCrNi austenites, owing to their substantially reduced nickel content.[12,13]

The nonmagnetic nature of the austenitic phase and its ability to maintain structural integrity at high temperatures are critical for applications requiring robust mechanical properties and resistance to thermal degradation. In addition, austenitic stainless steels are known for their good formability and weldability. The addition of nitrogen not only further stabilizes the austenite, but also increases mechanical strength and corrosion resistance without compromising the formability of the steel.[3,12]

1.4. Duplex Stainless Steels

Duplex stainless steels consist of a microstructure that combines both austenitic and ferritic phases, typically in a 50/50 ratio, although this can vary depending on the specific alloy composition. These steels utilize the FeCrNi system, with chromium content ranging from 18 to 28 mass% and nickel content ranging from 4.5 to 8 mass%. Additional alloying elements such as molybdenum (up to 5 mass%) and nitrogen are incorporated to enhance properties. The presence of molybdenum significantly increases resistance to chloride-induced pitting and crevice corrosion, while nitrogen contributes to increased mechanical strength due to solid solution strengthening and corrosion resistance, especially against local corrosion types such as pitting and crevice corrosion.[3,14–16] Similar to austenitic steels, there is ongoing research aimed at reducing or eliminating the content of the cost-intensive element nickel in duplex stainless steels. Kumar et al.[17] and Abdallah et al.[18] have developed various nickel lean or nickel-free duplex stainless steels, which demonstrate promising corrosion properties.[17,18]

The duplex structure in general provides an advantageous combination of properties derived from both the austenitic and ferritic phases. The ferritic phase provides high strength and resistance to stress corrosion cracking, particularly in chloride environments, while the austenitic phase contributes to improved toughness and ductility. This hybrid structure results in duplex stainless steels with higher strength and improved corrosion resistance compared to conventional austenitic and ferritic stainless steels, particularly in aggressive environments.[3]

1.5. Martensitic Stainless Steels

Martensitic stainless steels are characterized by a higher carbon content compared to the other types of stainless steels, typically ranging from 0.1 to 1.2 mass%. This class of steels is primarily based on the FeCrC system, with chromium contents typically ranging from 12 to 18 mass%.[3,19] The addition of carbon enables austenitizing and facilitates the formation of a martensitic crystal structure, whose formation involves a change from an austenitic phase to a martensitic phase upon rapid cooling, such as in water or oil. This process gives martensitic stainless steels a body-centered-tetragonal structure, which is responsible for their high strength. After quenching, these steels are typically tempered, which reduces the brittleness introduced during quenching and improves toughness.[3]

Martensitic stainless steels are ferromagnetic and have a good combination of high strength, wear resistance, and moderate

corrosion resistance. Their corrosion resistance is lower than that of austenitic and duplex stainless steels due to the higher defect density, the lower chromium content, and higher carbon content, leading to high susceptibility for chromium-rich $M_{23}C_6$ formation and thus intergranular corrosion. To improve their properties, elements such as nickel, molybdenum, and vanadium can be added to improve toughness (nickel), wear resistance (vanadium for the formation of VC carbides), and corrosion resistance (molybdenum for better pitting resistance).[3]

2. Nitrogen in Stainless Steels

Located next to carbon in the periodic table, nitrogen has an atomic diameter of 0.148 nm, which allows it to dissolve interstitially in the iron lattice.[19] When nitrogen is present as an interstitial solute, it contributes to an increase in mechanical strength through solid solution strengthening. At the same time, as noted above, nitrogen leads to an increase in resistance to pitting corrosion.[3,19] In addition, nitrogen serves to enhance the close-range ordering of substitutionally dissolved elements such as chromium, thereby mitigating the formation of chromium clusters, which are considered precursors to $M_{23}C_6$ carbide precipitation. Thus, nitrogen not only directly enhances corrosion resistance by the increase of pitting resistance, but also indirectly enhances the corrosion resistance of stainless steels by reducing the propensity for chromium-rich precipitation. Besides, when nitrogen interacts with chromium, it is predominantly precipitated in M_2N nitrides. This type of precipitation extracts less chromium from the matrix compared to $M_{23}C_6$ precipitation, thereby preserving the corrosion resistant properties of the steel.[3,19]

Similar to carbon, nitrogen has limited solubility in iron lattices, with the maximum solubility in ferrite (0.004 mass% at about 900 °C) being about 10 times lower than in austenite (0.045 mass% also at about 900 °C) due to the larger octahedral lattice vacancies in the austenitic fcc crystal.[20] Due to the low solubility in ferrite, the positive influences of nitrogen for ferritic stainless steels can hardly be utilized. For this reason, nitrogen is specifically alloyed only in austenitic, martensitic, and ferritic–austenitic (duplex) stainless steels. The content of interstitially soluble nitrogen, i.e., nitrogen solubility, in these steels can be adjusted by appropriate alloy design. Chromium, molybdenum, manganese, niobium, vanadium, tungsten, and titanium increase nitrogen solubility by reducing nitrogen activity, although only chromium and manganese are effectively used to increase solubility because the other elements tend to form nitrides due to their high affinity for nitrogen.[3,19]

The increase in strength due to interstitially dissolved nitrogen in austenitic steels follows the conventional strength–ductility trade-off only up to a certain limit. Wang et al.[21] through tensile testing of 316L(N) stainless steel with nitrogen contents varying up to 0.34 mass%, observed that elongation did not significantly decline beyond a specific nitrogen threshold (0.17 mass% in their study). This phenomenon may be attributed to the influence of nitrogen on the concentration of free electrons, as investigated by Shanina et al.[22] in CrMn austenites. Their findings indicated that nitrogen increases the number of free electrons, thereby enhancing the metallic bond character, which positively impacts ductility. This effect is especially pronounced when nitrogen coexists with interstitially dissolved carbon, as seen in C + N CrMn austenitic steels.[12,22,23]

Due to their high chromium content, duplex stainless steels contain considerable nitrogen contents of up to 0.2–0.35 mass%, which are mainly dissolved interstitially in the austenite in the phase mixture of 50 vol% ferrite and 50 vol% austenite due to the higher solubility in the austenitic fcc lattice. This partitioning means that only the austenitic phase in duplex stainless steels benefits from nitrogen alloying, which results in a good overall property profile of high strength and higher corrosion resistance already mentioned in Section 1.[16,19]

In martensitic stainless steels, nitrogen, like carbon, is soluble during austenitizing and contributes to the subsequent formation of martensite upon quenching. This contribution is of interest because the potential for hardness improvement by increasing carbon content is limited by a corresponding increase in the risk of $M_{23}C_6$ carbide precipitation, which increases the propensity for intergranular corrosion. The alloying with nitrogen offers a strategic advantage, allowing an increase in hardness while improving the corrosion resistance of the alloy, exceeding that of FeCrC martensitic stainless steels.[19,24] The increased presence of austenite-stabilizing elements, carbon and nitrogen, stabilizes retained austenite in the steel microstructure after quenching to room temperature. Managing this retained austenite often requires the implementation of freezing or deep cryogenic treatments subsequently to the quenching process.[19,25] These advanced methods are essential to convert the retained austenite to martensite, thereby increasing strength of the steel.

3. Manufacturing of High-Nitrogen Stainless Steels

The previous section shows that nitrogen has a positive influence on the properties of stainless steels. However, the production of nitrogen-alloyed steels is challenging. This is mainly due to the limited solubility of nitrogen in the steel melt which, if exceeded, leads to outgassing of N_2 (boiling of the melt) with loss of nitrogen and formation of pores.[19,26,27]

Nevertheless, there are several processing routes available to produce nitrogen-alloyed steels, including both melting and powder metallurgy (PM). In conventional metallurgy techniques such as the melting in an induction furnace nitrogen is introduced into the steel melt either by the addition of nitrogen-enriched ferroalloys or applying nitrogen-rich gas atmosphere. In this case, the achievable nitrogen content primarily depends on the chemical composition of the steel. For example, the steel X2CrNiMoN17-11-2 attains a nitrogen content of max. 0.22 mass%.[28] As described in the previous section, chromium and manganese enhance nitrogen solubility. Consequently, the steel X8CrMn18-18, with a similar processing method, achieves a nitrogen content of ≈0.55 mass%.[3]

In addition to the chemical composition, the prevailing N_2 partial pressure during melting also influences the nitrogen solubility according to Sieverts' law[29]

$$[\%N] = K_N \cdot \sqrt{p_{N_2}} \tag{3}$$

where K_N is a temperature-dependent constant that also accounts for the interaction of the steel's alloying elements with nitrogen.

This relationship indicates that the higher the N_2 partial pressure during the melting of steel, the greater the soluble nitrogen content. Consequently, pressure-assisted melting has proven to be an effective method for producing nitrogen-alloyed steels. A common pressure metallurgy process is pressurized electroslag remelting (PESR), which operates similar to the electroslag remelting (ESR) process, but under external pressure.[30–34] ESR works by using an electric current to melt a consumable electrode. The molten metal droplets pass through a layer of electrically conductive slag, which absorbs impurities from the metal. The purified molten metal then collects and solidifies in a water-cooled copper mold. The electrode is continuously lowered into the slag to maintain a uniform melting and solidification process.[3] The PESR process incorporates granulated nitrides such as Si_3N_4 into the slag as a nitrogen source and uses elevated pressures of up to 40 bar to increase nitrogen solubility according to Equation (3).[12,31]

While PESR faces the challenge of limited nitrogen solubility in the steel melt, the PM route avoids this problem by incorporating nitrogen in solid phase of the steel, where the nitrogen solubility is significantly higher than in the liquid phase. The basic process route for the production of high-nitrogen steels (HNS) presented in this article is based on the PM approach and is therefore specifically discussed in the next sections.[19]

4. New Powder Metallurgical Approach to Produce Austenitic HNS

In ref. [35], the authors of the present article have developed a new powder metallurgical approach for the production of HNS. As depicted in **Figure 1**, a powder mixture consisting of stainless steel and Si_3N_4, serving as the nitrogen donor, is encapsulated in a gas-tight steel capsule, and subsequently subjected to hot isostatic pressing (HIP). During the HIP process, at a high temperature and isostatic pressure ($T = 1200$ °C, $p = 150$ MPa), the Si_3N_4 particles are expected to dissolve, facilitating the diffusion of silicon and nitrogen into the steel matrix. As detailed in Section 3, this method circumvents the limited solubility of nitrogen in the molten state by exploiting its higher solubility in the solid state. What is new about this process route compared to other PM routes for the production of HNS is both the use of the nitrogen donor Si_3N_4, which has not previously been used in the course of diffusion alloying in the HIP, and in particular the use of a HIP with an integrated gas quenching (Uniform Rapid Quenching (URQ)) unit, which allows solution annealing of austenitic steels directly during the densification step.

The selection of Si_3N_4 as a nitrogen donor is attributed to the advantageous stoichiometry of this ceramic. With a nitrogen content of 40 mass%, Si_3N_4 possesses the highest nitrogen content among potential nitrogen donors in steels, such as Cr_2N, CrN, and Fe_2N. This provides the optimal opportunity to achieve nitrogen enrichment without significantly increasing the concentration of other elements, thereby avoiding deviations from the nominal alloying compositions due to mixing. The second significant difference from other PM routes is the use of a HIP system with URQ. As shown in the phase diagram in Figure 1, the isostatic pressure applied during HIP stabilizes the austenitic phase, which is associated with higher nitrogen solubility. The use of URQ allows this state to be maintained down to room

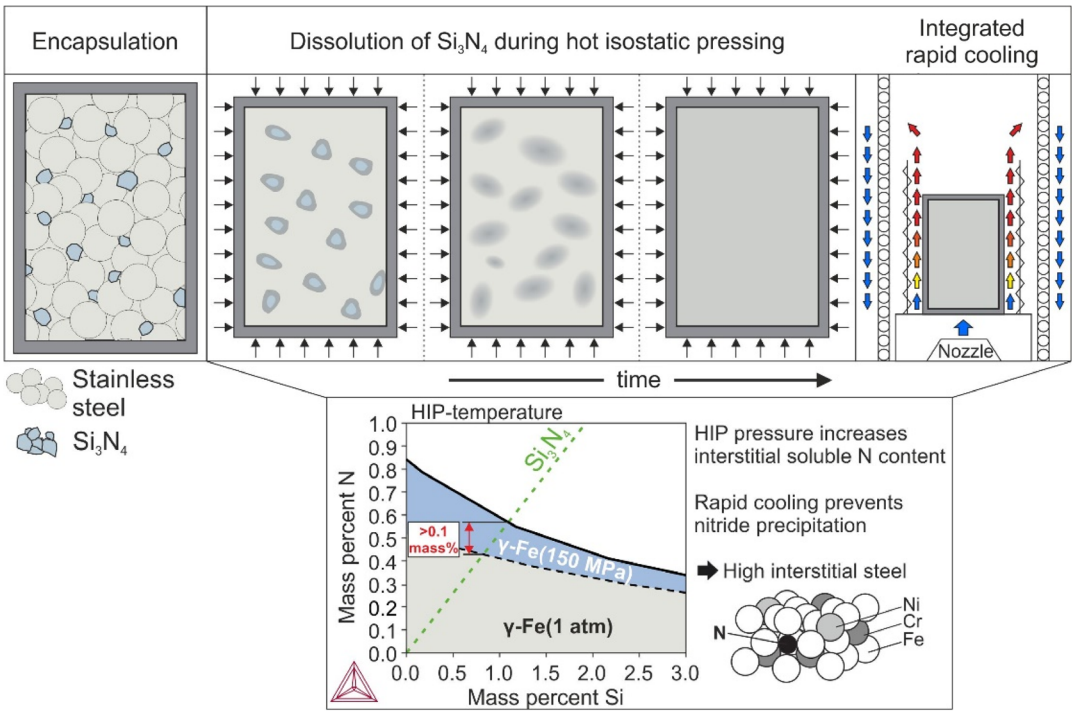

Figure 1. Illustration of the process sequence of the new approach for the powder metallurgical production of HNS by encapsulation of a powder mixture of stainless steel powder and Si_3N_4, HIP, and the associated dissolution of the Si_3N_4 particles and the resulting nitrogen enrichment of the matrix, as well as rapid quenching within the HIP. The isostatic pressure prevailing during HIP increases the stability of the austenitic phase, resulting in a higher interstitial soluble nitrogen content compared to atmospheric pressure. Reproduced with permission.[35] Copyright 2023, Materials Letters.

temperature, resulting in matrices that are highly supersaturated with nitrogen. This cannot be achieved with conventional PM methods, involving HIP followed by solution annealing at atmospheric pressure.

To investigate the feasibility of this approach, the study utilized X2CrNi18-9 stainless steel powder (particle size of 20–50 µm) and Si_3N_4 powder (particle size of 44–150 µm), containing ≈40 mass% nitrogen. By mixing 2.2 vol% Si_3N_4 and 97.8 vol% steel powder using a tumbling mixer, a target nitrogen content of 0.5 mass% was sought, which corresponds to the maximum nitrogen content thermodynamically soluble in austenite during HIP, according to thermodynamic calculations using the CALPHAD method. The HIP process was carried out at 150 MPa and 1200 °C, corresponding to the conditions considered for thermodynamic calculations, for 5 h, followed by rapid quenching with argon gas.

The scanning electron microscope (SEM) image in **Figure 2**a shows the formation of an austenitic matrix after HIP, with darker areas indicating local silicon enrichments. These enrichments correspond to the silicon distribution shown in Figure 2c, suggesting locations where Si_3N_4 dissolved during the HIP process. The resulting nitrogen content is 0.38 mass%, which is 0.07 mass% lower than the initial powder mixture's nitrogen content of 0.5 mass%. This slight decrease in nitrogen content from the powder can be attributed to nitrogen loss during HIP. This loss occurs due to the low N_2 partial pressure in the HIP compression gas, which creates a driving force for nitrogen to diffuse into the HIP atmosphere, trying to equalize the nitrogen gradient between the steel and the HIP atmosphere. Based on the silicon and nitrogen distribution in Figure 2c,d, few to no local enrichments are detected, which would indicate remaining Si_3N_4 particles. This suggests that nitrogen is primarily in interstitial solution within the matrix. Additionally, an inverse relationship between nitrogen and silicon distribution is observed, with higher silicon content corresponding to lower nitrogen content. This phenomenon is attributed to the nitrogen activity-enhancing effect of silicon. This also means that a homogeneous distribution of nitrogen is only achievable when silicon is uniformly distributed.

The results demonstrated that the PM process route shown in Figure 1 can be successfully employed for the production of HNS. In particular, the steel was produced solely by HIP without the need for additional solution annealing. The cooling rate achieved by the internal gas quenching in the HIP is sufficiently high to ensure that the nitrogen remains in interstitial solution and does not precipitate as nitrides during cooling.

4.1. Mechanical Properties

To evaluate the potential of the HNS processed according to the process route shown in Figure 1, fatigue tests were conducted. The objective of these tests was to model the high cycle fatigue (HCF) according to DIN 50 113 and to demonstrate the influence of nitrogen on the material's strengthening under cyclic loading. For fcc materials, it is not usual to characterize the finite life, as the stress (S) continuously decreases with an increasing number of load cycles (N), describing type 2 S–N curves.[36] Hence, the evaluation of HCF is sufficient for an assessment of cyclic strength increase. Additionally, the fracture surface allows to identify crack initiation sites and potential inclusions. For

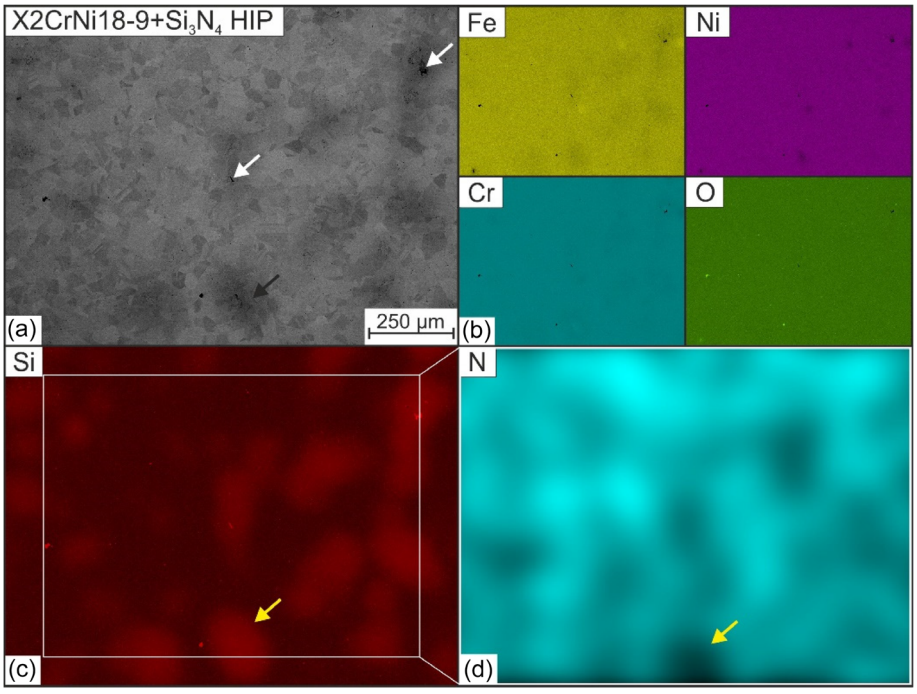

Figure 2. SEM investigation of the X2CrNi18-9 + Si_3N_4 material after HIP: a) secondary electron microscopic image (white arrows indicate silicon diffusion seams), b) distribution of Fe, nickel, chromium, and O, c) distribution of silicon, and d) distribution on nitrogen; all element distributions were measured by EDS.[35] Reproduced with permission.[35] Copyright 2023, Materials Letters.

instance, multiple crack initiation sites indicate a surface failure of the specimens. Single crack initiation sites at so-called fish-eye defects are often attributed to inclusions or pores and represent the material and processing quality.[37]

4.1.1. Experimental

Rotating bending tests ($R = -1$) were conducted at a frequency of 57.5 Hz. A forged and solution annealed material, X2CrNiN18-9, with a nitrogen content of 0.12 wt%, was used as the reference material. Eleven samples of the reference material and five samples of the HIP material were prepared according to **Figure 3**, manual longitudinal polished and tested in accordance with DIN 50 113. The sample size limitation due to the size of the HIP capsule explains the lower number of HIP material. For the evaluation of the HCF curve using the pearl string method, the software SAFD[38] was utilized.

A SEM of type JSM-6400 (JEOL Ltd.) was used to analyze the fracture surfaces. For topography characterization, a secondary electron (SE) detector was employed. To visualize inclusions, a backscatter electron (BSE) detector was used in combination with energy-dispersive X-ray spectrometry (EDS) point scans.

4.1.2. Results and Discussion

Obtained *S–N* curves are presented in **Figure 4**a where the applied stress amplitude is plotted against the number of cycles. Each failed specimen is represented by an unfilled circle. The calculation using the pearl string method is displayed as a fit within the diagram. The reference material, X2CrNiN18-9 (forged), is shown in black, while the PM HIP HNS X2CrNi18-9 + Si_3N_4 is shown in orange. The results indicate that the HNS material exhibits a clear increase in HCF strength, regarding higher fracture cycles and higher stress amplitudes. Additionally, the slope of the X2CrNi18-9 + Si_3N_4 HIP fit is less steep, suggesting a tendency toward a better long-life fatigue behavior. The 0.26 mass% increase in nitrogen content in the X2CrNi18-9 + Si_3N_4 HIP material, compared to the 304LN reference material, is hypothesized to significantly contribute to the observed optimization of fatigue properties. This hypothesis will be further evaluated in subsequent studies, where other critical factors such as grain size, inclusion density, and porosity will be systematically analyzed. Despite the need for further validation, the enhanced fatigue performance observed in the HCF regime demonstrates the significant potential of the investigated processing route to improve material behavior. However, due to the limited number of specimens, caution is required in interpreting the results, as no definitive conclusions regarding statistically significant values can be drawn at this stage.

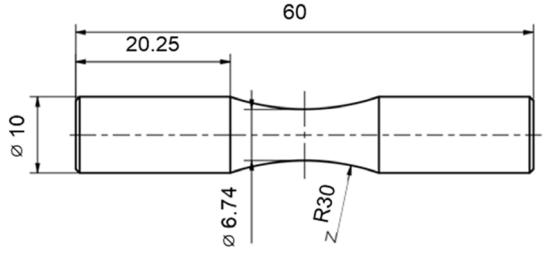

Figure 3. Specimen geometry for rotating bending tests, numbers given in mm.

A representative fracture surface of the reference material can be seen in Figure 4b. The specimen depicted here failed at a stress amplitude of 375 MPa after 187 000 cycles. A clear crack initiation site is visible in the SE detector image (red circle). The same specimen was imaged at higher magnification using a BSE detector (Figure 4c), where no notable defects such as inclusions or pores could be identified. This suggests that the failure was due to the inherent material behavior of the steel.

Figure 4d depicts a representative fracture surface of a X2CrNi18-9 + Si_3N_4 HIP specimen that failed at a stress amplitude of 400 MPa after 285 000 cycles. A clear crack initiation site is also visible in the SE detector image (red circle). Under higher magnification using the BSE detector, a distinct inclusion was observed. EDS point measurement of the dark colored area indicated a Ti–N-rich particle. This particle served as the crack initiation site and was thus critical to the failure. Similar inclusions with different amounts of Ti, Si, Al, N, and O were identified at the edge regions of all HIP specimen fracture surfaces. These inclusions can only be attributed to impurities in the powder material, either in the X2CrNi18-9 powder or the Si_3N_4 powder. To determine the source of the contamination, oxygen measurements were carried out on both types of powder using carrier gas hot extraction. The steel powder has an oxygen content of only 300 ppm, while the Si_3N_4 powder consists of ≈7000 ppm. This result drastically shows the importance of Si_3N_4 purity, the influence of oxygen contamination within the additive material, and the results on the microstructure and resulting properties.

A comparison of both materials clearly shows better cyclic strength of the X2CrNi18-9 + Si_3N_4 HIP material, despite the existence of large nonmetallic inclusions which act as crack starting points. This indicates a rather poor degree of purity of the PM grade. Therefore, it can be assumed that the intrinsic fatigue strength of the HIP material is significantly higher than represented here. The new PM process approach depicted in Figure 1 demonstrates a positive effect on the strength of cyclically loaded components. As usual for high-strength materials, the fatigue resistance is limited by impurities, acting as defects in a fracture mechanical sense. These impurities not only influence the mechanical properties but may also affect the corrosion behavior. Since corrosion resistance is a primary focus for stainless steels, the impact of the detected nonmetallic inclusions on corrosion behavior will be assessed in future studies. It can already be concluded that the material properties have not yet reached their maximum potential, primarily due to the significant contamination of Si_3N_4 with oxygen.

5. Transferability of the New Approach to Additive Manufacturing of Austenitic HNS

5.1. Motivation

Additive manufacturing (AM) has revolutionized industrial manufacturing by enabling the production of complex geometries and customized parts with high precision and efficiency. This technology reduces material waste and production time

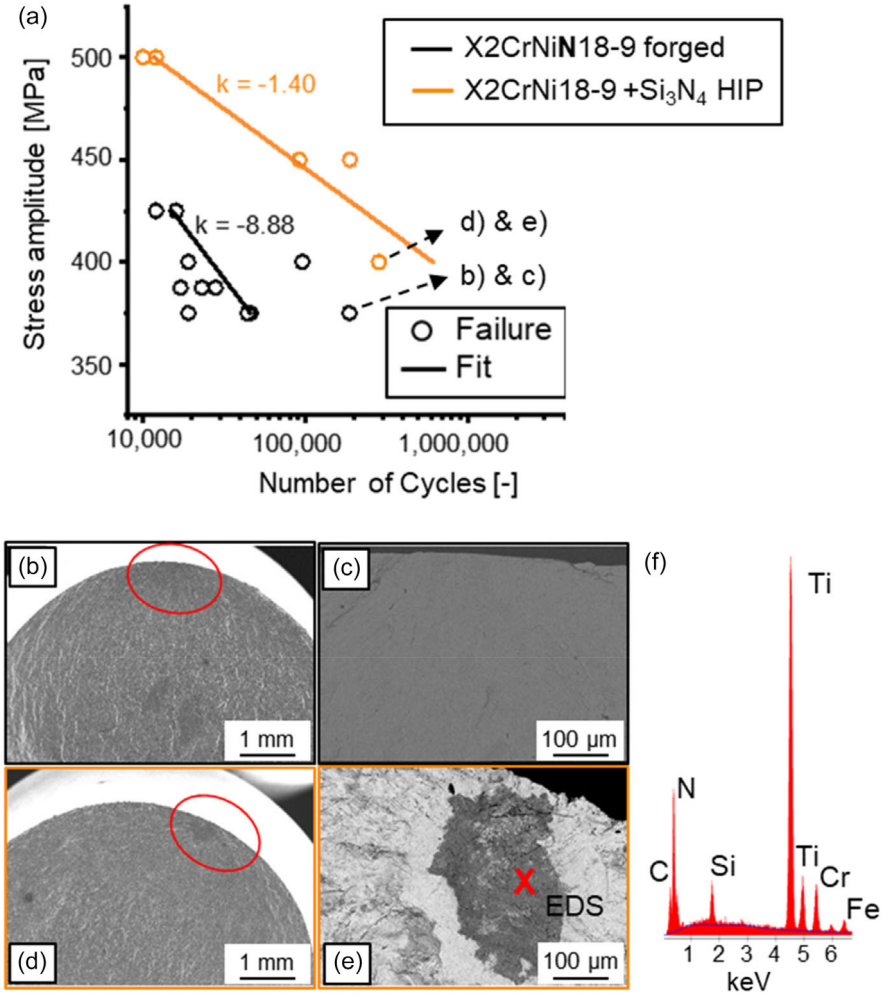

Figure 4. a) S–N curves of the rotating bending test for X2CrNiN18-9 forged reference material and X2CrNi18-9 + Si_3N_4 HIP material, b) SE image of X2CrNiN18-9 forged fracture surface, c) BSE image of X2CrNiN18-9 forged fracture surface, d) SE image of X2CrNi18-9 + Si_3N_4 HIP fracture surface, e) BSE image of X2CrNi18-9 + Si_3N_4 HIP fracture surface, and f) qualitative EDS point scan of detected inclusion inside of X2CrNi18-9 + Si_3N_4 HIP fracture surface.

compared to traditional manufacturing methods, offering significant cost savings and flexibility. The ability to produce intricate designs and functional prototypes directly from digital models accelerates innovation and reduces time-to-market for new products.[39,40]

Despite its advantages, the widespread adoption of AM in the metal sector necessitates ongoing research into new materials. Developing advanced metal alloys specifically tailored for AM processes is crucial to overcoming challenges such as residual stresses, microstructural defects, and limited material properties. Research in this area aims to enhance the mechanical performance, durability, and reliability of AM-processed metal parts, ensuring they meet the stringent requirements of industries such as aerospace, automotive, and medical devices.[41,42]

Powder bed fusion of metals using a laser beam (PBF-LB/M) is one category of AM processes that uses a laser beam to selectively melt and fuse thin layers of metal powder, creating 3D parts. The process begins with a thin layer of metal powder spread across a build platform. A laser beam, directed by a high-precision scanning system, selectively melts the powder according to the CAD data of the part. Once a layer is completed, the build platform lowers, and a new layer of powder is applied. This cycle repeats until the part is fully constructed.[39,43] This process creates small melt pools that are significantly smaller in volume than the build platform or the already processed component. This leads to rapid heat dissipation, resulting in high solidification and cooling rates. These conditions generate significant thermal stresses that can cause distortion or cracking of the part.[44] When it comes to steels, not every alloy can withstand these harsh thermal conditions. Therefore, materials commonly used in welding, such as the austenitic steel X2CrNiMo17-12-2, are preferred due to their high tolerance to thermal stresses. The steels currently utilized in AM often lack the requisite mechanical and chemical properties to meet the generally demanding requirements of industrial applications.[45]

For this reason, research is being conducted on new materials and process routes for the AM of steels to achieve optimal

PBF-LB/M processability, along with enhanced chemical and mechanical properties. In the area of the aforementioned austenitic steels, the alloying element nitrogen is often a focal point due to its significantly positive influence on the mechanical and chemical properties of stainless steels.[41]

To date, the nitrogen content achievable in PBF-LB/M-produced steels has been constrained by the maximum nitrogen solubility in the melt of the respective steel. Boes et al.[46] achieved a nitrogen content of 0.58 mass% in the X2CNiMo17-12-2 stainless steel powder by gas nitriding. They adjusted a nitrogen content of ≈0.1 mass% (0.1N) and 0.3mass% (0.3N) by mixing with untreated powder, and subsequently processed these powder mixtures using PBF-LB/M in an N_2 process atmosphere. In the 0.1N powder, a sample density greater than 99.7% was achieved, while the nitrogen content slightly increased compared to the powder. These results were attributed to the nitrogen content of 0.1 mass% in the powder not exceeding the nitrogen solubility limit. On the contrary, this level had not yet been reached, allowing the melt to absorb additional nitrogen from the dissociation reaction of N_2 from the process atmosphere. In contrast, the 0.3N powder exhibited a significant nitrogen loss in the PBF-LB/M samples compared to the powder, along with the formation of gas pores. This was attributed to exceeding the nitrogen solubility limit in the melt. Regarding mechanical properties, higher strength was observed in both nitrogen-alloyed X2CrNiMo17-12-2 variants compared to the nitrogen-free base material. However, the increased porosity of the 0.3N steel resulted in significant reductions in elongation at fracture.[46]

5.2. Initial Approach

Due to the limited solubility of nitrogen in the steel's liquid phase, the authors of the present work sought to transfer the powder metallurgical approach for producing HNS, as detailed in ref. [35] and explained in Section 3, to PBF-LB/M of HNS. The process sequence is depicted in **Figure 5**. It includes the processing of a powder mixture of steel powder and Si_3N_4 by PBF-LB/M. The objective during production is to obtain the Si_3N_4 particles within the laser-consolidated steel matrix and subsequently dissolve them in the solid phase during HIP, in accordance with the observations in ref. [35]. This approach circumvents the limited nitrogen solubility in the melt, thus enabling the AM of steels with nitrogen contents far above their maximum nitrogen solubility in the liquid phase. The first findings on this approach were collected in refs. [47,48].

As starting materials for the process route, two powders were utilized: the base steel powder (X2CrNi18-9) and a nitrogen additive (Si_3N_4). As illustrated in Figure 5, the particle interaction during recoating was investigated. The additively built sample was intended to consist of residual Si_3N_4 particles and closed porosity, which would facilitate the diffusion alloying of nitrogen and the postdensification of pores formed during PBF-LB/M within the HIP process. In comparison with the HIP route, AM imposed stricter requirements on the powder properties. Therefore, the flow properties, bulk density, moisture content, and laser absorption were investigated and optimized.

During the AM step, two main objectives were pursued. First, it was essential to avoid complete decomposition of the Si_3N_4 particles to ensure nitrogen diffusion during the HIP process. Premature release of all the nitrogen from the Si_3N_4 powder particles would have resulted in solubility issues, as described in the literature. Consequently, the particle size distribution of the Si_3N_4 powder was kept as coarse as possible to minimize dissolution. The second objective was the fabrication of gas-tight specimens. To ensure a successful densification during HIP, the component had to exhibit no open porosity. Once a relative density of 95% was achieved, it was assumed that only closed porosity was present.[49,50]

Investigations into the powder properties demonstrated that the addition of Si_3N_4 deteriorated the flowability compared to the base powder. However, the moisture content and laser absorption of the powder remained unaffected. By varying the particle size distribution of the additive and the mixing methodology, sufficiently flowable mixtures were produced.[47]

In ref. [48], the authors investigated the processability of X2CrNi18-9 + Si_3N_4 compared to pure X2CrNi18-9 powder. The addition of Si_3N_4 powder significantly reduced the processability and reproducibility of dense samples. The intended

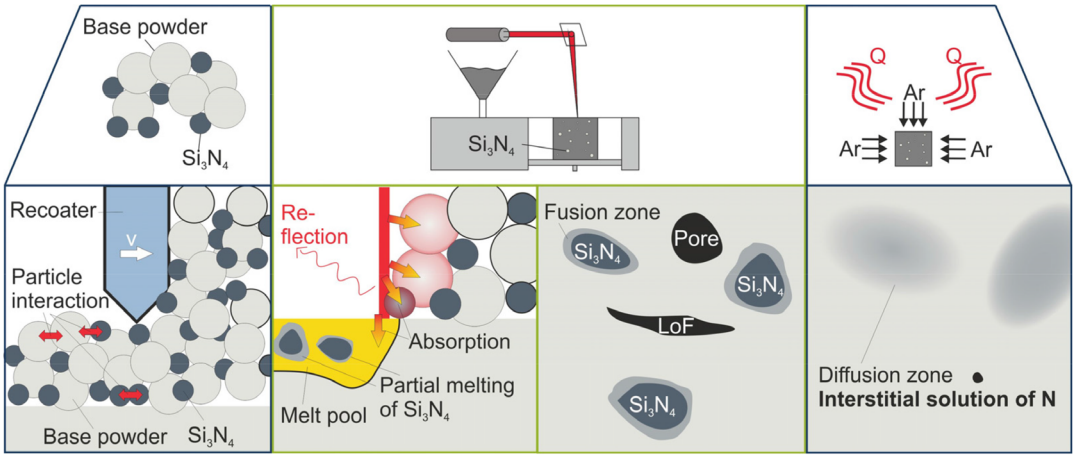

Figure 5. Illustration of the process route of the new approach for the AM of HNS by using an additivated powder with Si_3N_4, aiming for unmelted Si_3N_4 particles inside a steel matrix. Using a HIP postprocess for diffusion alloying of the additive manufactured parts.

(a)	X2CrNi18-9		X2CrNi18-9 + Si_3N_4	
	Powder	PBF-LB/M	Powder	PBF-LB/M
N content [mass%]	0.084 ± 0.008	0.078 ± 0.011	0.446 ± 0.020	0.085 ± 0.007

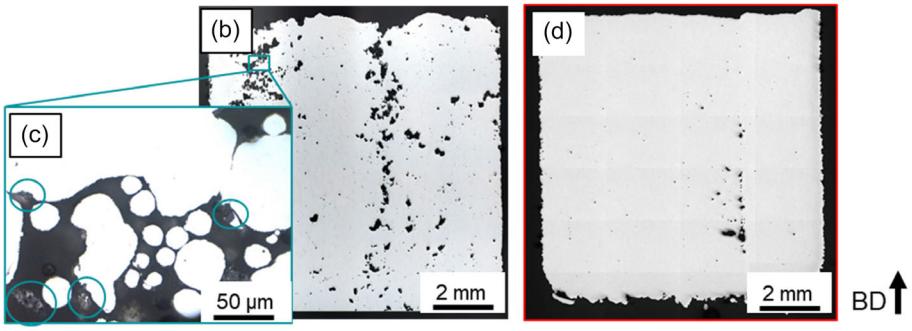

Figure 6. Nitrogen contents for X2CrNi18-9 powder and PBF-LB/M samples: a) X2CrNi18-9 + Si_3N_4 powder and PBF-LB/M samples (measured by carrier gas hot extraction), b) light microscopic sections of a highly porous specimen, c) revealing remaining Si_3N_4 particles inside of defects, and d) dense specimen without remaining Si_3N_4 particles.

increase in the nitrogen content up to 0.45 mass% due to residual Si_3N_4 particles was not achieved (**Figure 6**a). After processing a gas-tight sample (Figure 6d), a nitrogen loss of 0.361 mass% was measured, resulting in the same chemical composition as the pure X2CrNi18-9 powder (0.085 mass%). The unexpected production of high porosity samples (Figure 6b) revealed residual Si_3N_4 particles inside voids and gaps between hatches (Figure 6c). The poor powder flowability resulted in high variability in pore structure and an inhomogeneous distribution of defects, causing processing issues but increasing the locally Si_3N_4 content. The present study revealed that the two primary requirements, maintaining coarse Si_3N_4 particles during PBF-LB/M and producing gas-tight samples, were contradictory.

5.3. Adapted Approach

The aforementioned observations led to the development of an adapted approach, namely, the PBF-LB/M production of shell–core samples from the powder mixture of stainless steel and Si_3N_4, which was published in ref. [51]. In the shell–core approach, the PBF-LB/M component is composed of a dense (fully exposed) shell and a completely (unexposed) or partially powdered (partially exposed) core. The full densification is subsequently achieved by HIP. In the context of the presented endeavor, this approach ensures the retention of Si_3N_4 particles within the PBF-LB/M component (see **Figure 7**), which dissolve during the subsequent HIP step. This approach should facilitate the AM of stainless steels with nitrogen contents exceeding the maximum nitrogen solubility in the melt.

The feasibility of this approach was demonstrated in ref. [51]. The results demonstrated that the HIP process ($T = 1200$ °C, $p = 150$ MPa, $t = 5$ h; same parameters as in ref. [35]) was highly effective in achieving near-complete densification of the shell–core samples. **Figure 8**a shows a cross section of the shell–core sample before HIP, and Figure 8b displays the sample after HIP. The initial structure features a dense shell surrounding a minimally exposed core, which transforms into an almost fully dense post-HIP structure. The shrinkage observed is due to the isostatic

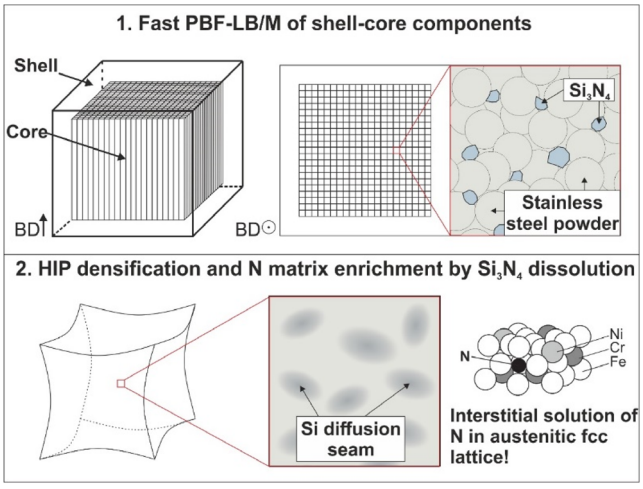

Figure 7. Shell–core approach for the AM of HNS published in ref. [51]. Reproduced under the terms of the CC BY 4.0 license.[51] Copyright 2024, The Authors. Published by Additive Manufacturing Letters.

pressure applied during HIP, which compresses the sample uniformly from all directions, ensuring the elimination of residual porosity and enhancing the material's density to more than 99.9%.

Figure 8c provides a close-up optical micrograph (OM) of the core structure before HIP, revealing a strut-like arrangement of laser consolidated volumes. Between these struts, loose powder is present after PBF-LB/M and before HIP, respectively. Figure 8d shows the silicon distribution in the HIP-densified sample, highlighting silicon diffusion seams, also arranged in a strut like manner. These seams are indicative of Si_3N_4 particles that remained in the powder regions after PBF-LB/M and dissolved during HIP, releasing nitrogen and silicon into the matrix in the same way as it was already shown in work[35] and Section 4. The electron backscatter diffraction scan, as shown in Figure 8e,f, confirmed a fully austenitic matrix with a typical austenitic grain structure characterized by equiaxed and twin grains.

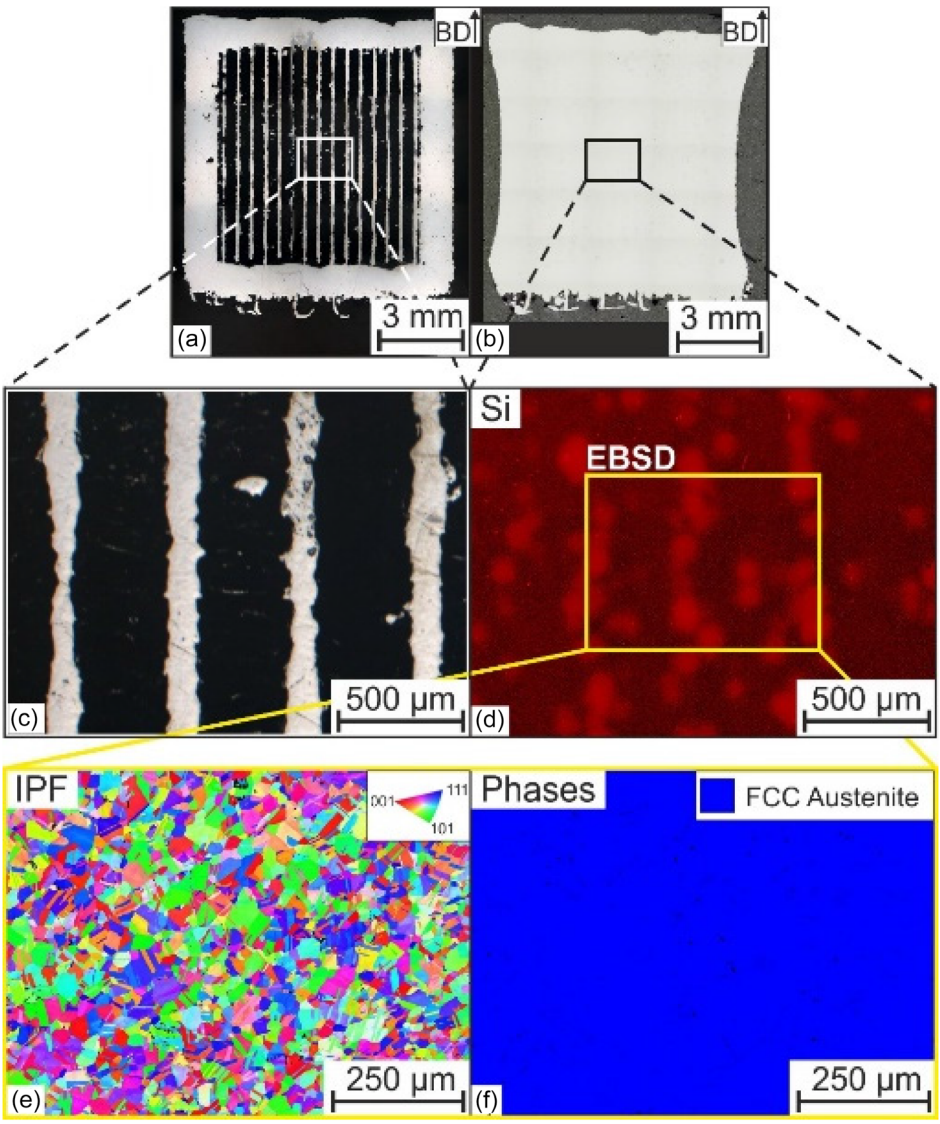

Figure 8. Microstructural investigations from ref. [51]: a) OM of shell–core sample before HIP and b) after HIP, c) close-up of the core, d) silicon distribution in the core, e) inverse pole figure map of a section from (d) and f) phase map corresponding to the map in (e). Reproduced under the terms of the CC BY 4.0 license.[51] Copyright 2024, The Authors. Published by Additive Manufacturing Letters.

In the laser-exposed areas, i.e., both in the shell and in the struts located in the core, no significant changes in nitrogen and silicon content could be detected after PBF-LB/M (before HIP) compared to the X2CrNi18-9 starting powder. This indicated that the laser interaction with the Si_3N_4 powders did not lead to the melting of the particles and the associated silicon and nitrogen enrichment of the steel, but to a decomposition reaction and the subsequent transfer of silicon and nitrogen into the process atmosphere. This led to the conclusion that only the Si_3N_4 particles remaining in the loose powder areas were available for diffusion alloying with silicon and especially nitrogen during HIP, as evidenced by the strut-like formation of silicon diffusion seams in Figure 8d. This also resulted in a significantly lower nitrogen content of the shell–core samples compared to the powder, which is consistent with the results shown in Section 5.2. After PBF-LB/M, the laser-induced decomposition reaction of the Si_3N_4 particles resulted in a nitrogen content of 0.24 mass% (compared to 0.45 mass% in the powder mixture of X2CrNi18-9 and Si_3N_4), which was further reduced to a value of 0.19 mass% after HIP. This latter nitrogen loss during HIP was attributed to the low nitrogen partial pressure in the HIP compression gas, which acted as a nitrogen sink and thus provided a driving force for nitrogen to diffuse from the steel into the HIP atmosphere.

In ref. [35], only the averaged, global nitrogen content was measured. In contrast, in the investigation of PBF-LB/M production of HNS utilizing the shell–core approach, the localized silicon and nitrogen content was quantified using microprobe analysis. This study emphasized the variations in silicon and nitrogen content between the shell and the core, as well as

the relationship between local silicon gradients and nitrogen content within the core. Additionally, nanoindentation was conducted to correlate chemical gradients with the local mechanical properties.

To investigate the differences in nitrogen and silicon content between the shell and core, a wavelength dispersive spectrometry (WDS) line scan was conducted from the sample's outer shell to the core, followed by a nanoindentation line scan at the same location to establish the correlation between local elemental content and nanohardness. The results, depicted in **Figure 9**a, show that the nitrogen content within the core remained almost constant at 0.24 mass%, decreasing toward the surface to a minimum of 0.11 mass%. The silicon profile displayed a nonlinear or irregular trend within the core, indicating silicon diffusion seams as observed in Figure 8d. Similar to nitrogen, the silicon content in the shell gradually decreases toward the surface. Nanohardness decreases within the shell toward the sample surface and stabilizes within the core at 3.1 GPa in the core.

The observed nitrogen and silicon distributions and the relationship with nanohardness could be explained as follows.

In the shell, a consistently low silicon and nitrogen content can be assumed after PBF-LB/M and before HIP, as the Si_3N_4 particles present in this region decompose primarily due to interaction with the laser during PBF-LB/M. During HIP, the Si_3N_4 particles located in the core, particularly in the remaining loose powder areas, dissolve, leading to the diffusion of silicon and nitrogen into the austenitic matrix. This results in a global silicon and nitrogen concentration difference between the shell and core, with a resulting driving force for silicon and nitrogen diffusion from the core into the shell. The diffusion rate of silicon is not sufficient to equalize the silicon concentration between the shell and the core, as evidenced by the decreasing silicon content detected in the shell in Figure 9b. The situation is different for nitrogen. Nitrogen has a sufficiently high diffusion rate that the gradient between the shell and the core could equalize. However, as described above, the HIP atmosphere acts as a constant nitrogen sink, with nitrogen passing from the steel into the HIP atmosphere. This was assumed to be one of the reasons for the gradient in the shell found for nitrogen. Nanohardness is directly correlated to the silicon and nitrogen contents measured in the core and shell. Lower nitrogen and silicon contents are associated with lower nanohardness due to lower solid solution strengthening. This is also the reason why the macrohardness is significantly lower in the shell (163 HV10) than in the core (182 HV10).

To determine the influence of silicon gradients on the nitrogen distribution as well as on the nanohardness in the core, EDS/WDS and subsequently nanoindentation line scans were conducted. **Figure 10**a shows the silicon distribution, highlighting silicon seams and bright silicon-rich particles, which are silicon- and manganese-rich oxides. The WDS line scan through a silicon diffusion seam in Figure 10a revealed an inverse segregation of nitrogen and silicon. The nitrogen content reached its lowest value of 0.17 mass% where the silicon content was highest (3.17 mass%) and its highest value of 0.24 mass% where the silicon content was lowest at 0.73 mass%. This inverse segregation is due to the mutually enhancing effects of nitrogen and silicon on their respective activities in the austenitic phase, already mentioned in Section 4.

Figure 9 demonstrates that varying nitrogen and silicon contents determined the differences in mechanical properties between the shell and the core. However, in Figure 10b, a nanoindentation line scan through several silicon diffusion seams in the core revealed no significant local differences in nanohardness. Thus, the inverse segregations of silicon and nitrogen within the core shown in Figure 10a do not significantly affect local mechanical properties. The solid solution strengthening contributions of both silicon and nitrogen compensate for each other; in regions with lower nitrogen content and higher silicon content within a silicon diffusion seam, silicon compensates for the reduced nitrogen content, resulting in a consistent nanohardness profile throughout the core. This contrasts with the nanohardness differences between the core and the shell, where both lower silicon and nitrogen contents lead to lower nanohardness in the shell.

The results from this study indicated that the proposed AM approach for HNS using the shell–core strategy is fundamentally promising. However, several challenges were identified: 1) The nitrogen content in the component after HIP is significantly lower than in the initial powder mixture of X2CrNi18-9 and Si_3N_4. This reduction is attributed to Si_3N_4 decomposition during PBF-LB/M and nitrogen effusion during HIP and 2) Localized silicon gradients result in an uneven distribution

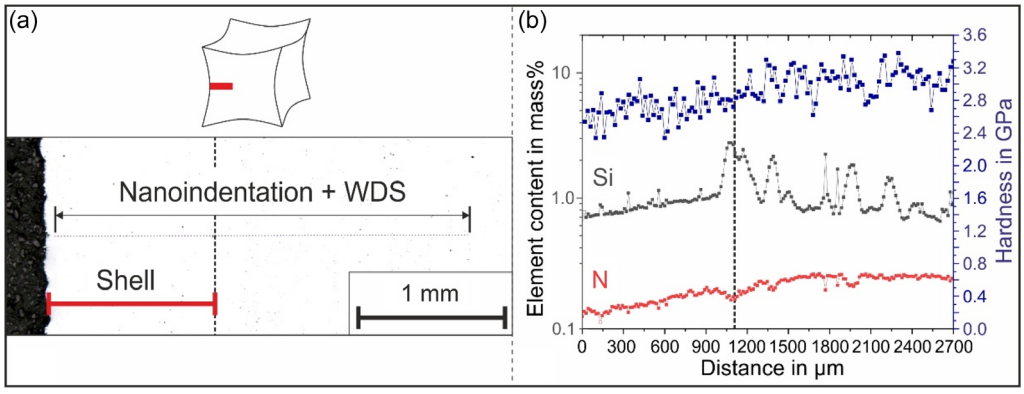

Figure 9. Nanohardness, silicon, and nitrogen course in a shell–core sample, beginning at the surface and continuing to the core: a) location of the measurements and b) nitrogen, silicon, and nanohadness profiles. Reproduced under the terms of the CC BY 4.0 license.[51] Copyright 2024, The Authors. Published by Additive Manufacturing Letters.

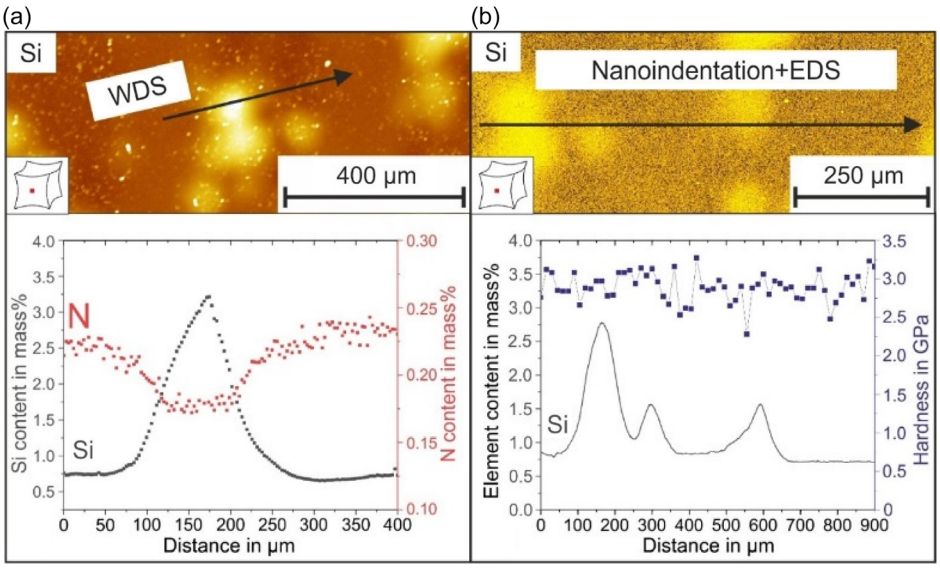

Figure 10. a) Silicon and nitrogen distribution in a silicon diffusion seam measured by WDS. b) Silicon distribution and hardness through several silicon diffusion seams.[51] Reproduced under the terms of the CC BY 4.0 license.[51] Copyright 2024, The Authors. Published by Additive Manufacturing Letters.

of nitrogen, potentially negatively impacting corrosion performance.

These findings highlight two key optimization potentials: 1) Reducing the laser-exposed volumes to preserve a higher proportion of Si_3N_4 in the powder regions and 2) Utilizing finer Si_3N_4 powder is intended to shorten the diffusion pathways for silicon and nitrogen by reducing interparticle distances. This, together with the faster dissolution of smaller Si_3N_4 particles, could facilitate improved homogenization of silicon and consequently nitrogen during the HIP process.

5.3.1. Optimization of the Approach

These optimization approaches were addressed in ref. [52] by increasing the hatch distance in the core from 500 to 600 µm (reducing laser exposed volumes in the core) and using Si_3N_4 particles smaller than 36 µm instead of a size in between 36 and 72 µm. In addition, ball milling was used to break up Si_3N_4 agglomerates and mechanically bond the fine particles to the steel particle surface, as indicated in **Figure 11**. Ball milling was used for the fine Si_3N_4 particle fraction smaller than 36 µm to improve the binding behavior and thus the powder properties as shown in ref. [47]. The mixing was carried out for 24 h, using WC grinding balls, and a medium rotation speed. The ball to powder ratio was 1:1 (vol%) with a vial filling factor of 66.7%.

Microstructural investigations shown in **Figure 12** revealed that the HIP-densified shell–core sample achieved almost 100% densification, which is accordance to the findings in Figure 8 or in ref. [51]. Elemental distribution analysis of silicon after HIP densification showed silicon diffusion seams analogous to the findings in Figure 8 or in ref. [51], indicating where Si_3N_4 particles dissolved during HIP. The strut-like pattern observed in the micrograph corresponded to areas of silicon diffusion, suggesting that the laser-exposed areas experienced a loss

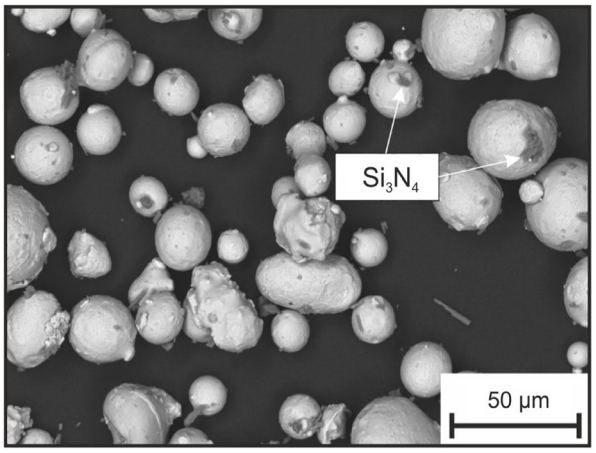

Figure 11. Powder mixture of X2CrNi18-9 + Si_3N_4 with an Si_3N_4 fraction smaller than 36 µm after ball milling for 24 h. Reproduced with permission.[52] Copyright 2024, Euro PM 2024.

of silicon and nitrogen due to Si_3N_4 decomposition, a finding consistent with the observations in ref. [51].

Further, the presence of silicon diffusion seams correlated with the local evolution of grain size. Areas with higher silicon diffusion seam density exhibited smaller grain sizes (20 ± 8 µm) compared to areas with lower density (50 ± 12 µm). The total grain size was 20 ± 15 µm, which was 19% larger than the grain size reported in ref. [51] for materials with coarser Si_3N_4 particles. This suggested that smaller Si_3N_4 particles dissolved more quickly during HIP, reducing their impact on grain growth inhibiting.

The total nitrogen content in the optimized shell–core sample after HIP was measured at 0.286 ± 0.005 mass%, indicating a 0.17 mass% nitrogen loss from the powder mixture. This

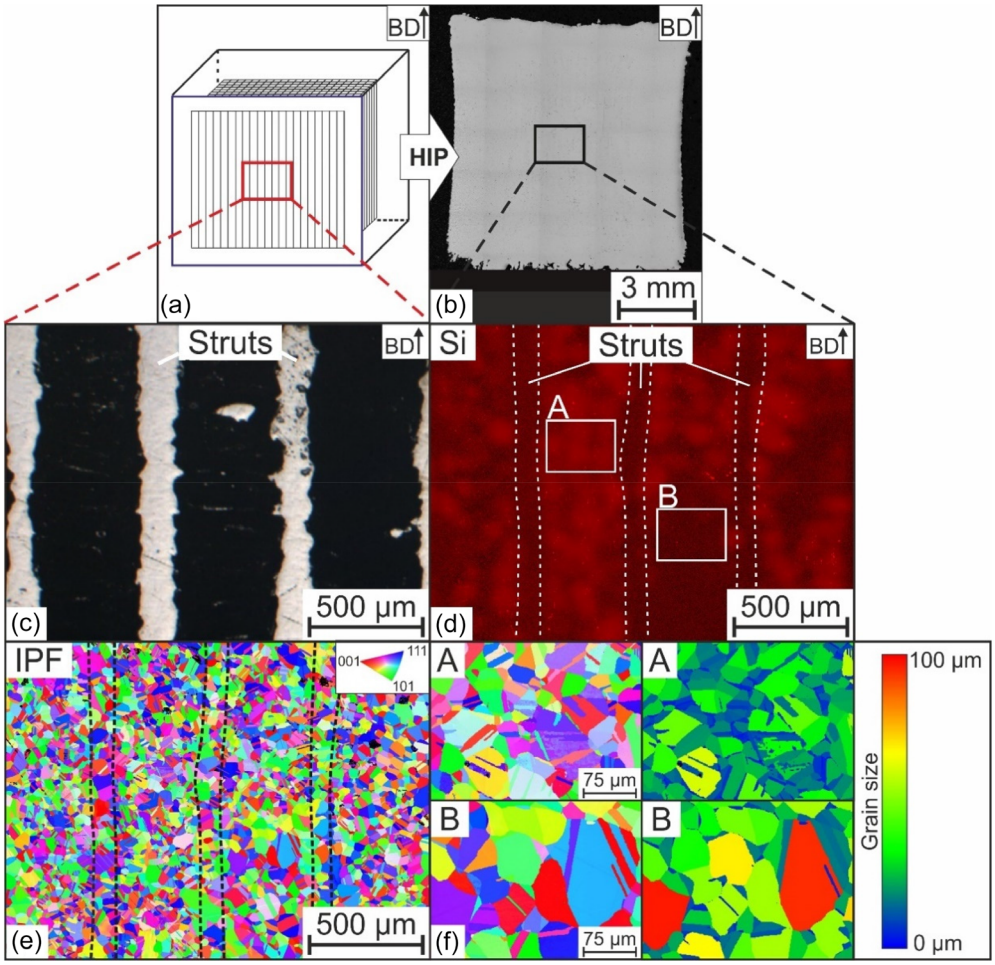

Figure 12. Microstructural investigations from ref. [52]: a) schematic illustration of shell–core sample before HIP, b) OM micrograph of the shell–core sample after HIP, c) close-up of the core, d) silicon distribution in the core, e) inverse pole figure map of the section from (d), and f) phase and grain size map corresponding to the marked section A and B indicated in (d). Reproduced with permission.[52] Copyright 2024, Euro PM 2024.

nitrogen loss was attributed to Si_3N_4 decomposition in laser-exposed areas during PBF-LB/M and nitrogen effusion into the HIP atmosphere. Compared to the previous study (nitrogen content of 0.18 mass% after HIP), the optimized process resulted in a higher nitrogen content. The improved nitrogen content with smaller Si_3N_4 particles was attributed to better mechanical adhesion of Si_3N_4 to the steel particles, reducing segregation during powder handling and application on the build platform. The higher nitrogen content in the shell–core sample led to higher hardness in the core (193 ± 6 HV10) and shell (164 ± 2 HV10) areas, compared to ref. [51], where hardness was 182 HV10 in the core and 163 HV10 in the shell. The increased hardness was linked to the higher interstitial nitrogen content and improved solid solution strengthening.

Additionally, the finer Si_3N_4 particles resulted in higher silicon homogeneity during HIP, with a 50% increase compared to coarser particles, which was evaluated by variograms based on quantitative silicon elemental distributions. This is also associated with a more homogeneous nitrogen distribution due to the inverse segregation behavior revealed by Figure 10.

In conclusion, the optimization of the AM process using finer Si_3N_4 particles and milling ball-assisted mixing significantly improved the nitrogen content and silicon homogeneity in the HIP-densified shell–core samples compared to the previous study.

6. Summary

This article presented a novel powder metallurgical approach for fabricating HNS via HIP of a powder mixture consisting of stainless steel powder and Si_3N_4. Additionally, it emphasized the application of this method to produce HNS in the framework of AM, specifically via the PBF-LB/M process.

First, the feasibility of the approach was demonstrated using the example of conventional PM-HIP production of the X2CrNi18-9 + Si_3N_4 system with a total nitrogen content of 0.38 mass%, which was published in ref. [35]. It was demonstrated that Si_3N_4 dissolves during HIP as intended and that the austenitic matrix is enriched with silicon and nitrogen.

The HIP-integrated gas quenching prevented nitride formation during cooling, allowing densification and solution annealing to be completed in one single step within the HIP. The fatigue properties of the steels produced by the above process showed significantly better performance in the high-cycle fatigue range compared to conventionally produced X2CrNiN18-9 steel. This was attributed to the enhanced solid solution strengthening effect resulting from the higher nitrogen content, underscoring the remarkable potential of the process route under consideration. To transfer the approach to the PBF-LB/M production of HNS, an initial attempt was made to produce an approximately dense microstructure from an X2CrNi18-9 + Si_3N_4 powder mixture in which Si_3N_4 is present as a ceramic phase in the laser-consolidated matrix. However, it was observed that during the interaction of the Si_3N_4 particles with the laser, a decomposition reaction occurred, leading to the loss of both silicon and nitrogen. Consequently, the shell–core strategy, in which a dense shell is fabricated around a minimally exposed core, was employed in ref. [51]. This process enabled the preservation of loose Si_3N_4 particles within the PBF-LB/M components, which subsequently dissolved during the HIP process. This dissolution was analogous to that observed in ref. [35], and it enriched the matrix with nitrogen. These observations indicated the feasibility of transferring the investigated approach to the fabrication of HNS in PBF-LB/M.

Significant differences were observed in the selection of two distinct Si_3N_4 fractions. In samples produced with a Si_3N_4 fraction smaller than 36 µm, there was a higher absolute nitrogen content compared to a Si_3N_4 fraction of 36–72 µm, leading to higher hardness. This was attributed to the occurrence of lower Si_3N_4 powder segregation processes during the PBF-LB/M powder application. Furthermore, a more homogeneous distribution of silicon was observed, with this distribution being directly correlated with the distribution of nitrogen. Locally increased silicon contents resulted in locally reduced nitrogen contents due to the nitrogen activity-enhancing effect of silicon.

6.1. Optimization Approaches

The following optimization approaches are presented, which will be pursued further in the future: 1) The use of smaller Si_3N_4 particles (nanometer range) for optimized silicon homogenization and thus an even more homogeneous nitrogen distribution. Furthermore, an Si_3N_4 powder with a lower O content is to be found for future investigations to minimize oxide formation during HIP; and 2) Use of a shapable laser (donut laser): During the production of PBF-LB/M, Si_3N_4 decomposes as a result of interaction with the laser. To obtain Si_3N_4 particles in the laser-exposed areas, it will be investigated in the future whether a weakened laser intensity profile can lead to a lower decomposition tendency of Si_3N_4 due to lower peak temperatures.

7. Outlook

The investigations demonstrate the fundamental feasibility of diffusion alloying with Si_3N_4 in a HIP with internal gas quenching for the production of HNS. Moreover, they proof the potential for transferring this approach to the PBF-LB/M process for HNS production, thereby effectively overcoming limitations in nitrogen content that arise from the restricted nitrogen solubility in the melt. While the feasibility has been demonstrated in this article using an austenitic CrNi steel, the approach can be applied to other groups of stainless steels presented in Section 1, such as martensitic, duplex, and austenitic stainless steels based on an alloy system other than the CrNi system. Due to the high levels of interstitially soluble nitrogen that can be achieved using this approach, the amount of nickel or manganese required for stabilizing austenite in the production of duplex and austenitic stainless steels can be entirely substituted with nitrogen. Consequently, it becomes feasible to produce these types of steels using only the FeCr(Si)N alloy system. This alloy system is also applicable to the production of martensitic stainless steels. The following discussion will explore the potential for manufacturing austenitic, duplex, and martensitic stainless steels using the FeCr(Si)N alloy system and the process methodology described in the present work.

7.1. Austenitic Stainless Steel

Figure 13 shows the isothermal phase diagram calculated using the CALPHAD method and considering the HIP conditions ($T = 1200\,°C$, $p = 150\,MPa$) for the Fe20Cr system, with the nitrogen content plotted against the silicon content. Additionally, the stoichiometric line of Si_3N_4 is marked, indicating in which amounts the nitrogen and silicon contents can be adjusted through Si_3N_4 addition. The Si_3N_4 line intersects the single-phase austenitic phase region within a nitrogen content range of ≈0.58–0.9 mass%, with corresponding silicon contents of 0.87–1.35 mass%. Assuming the thermodynamic equilibrium state is achieved during HIP, the appropriate addition of Si_3N_4 would result in the formation of a single-phase austenitic structure, which could be maintained down to room temperature through HIP-internal gas quenching. To achieve this, sufficient austenite

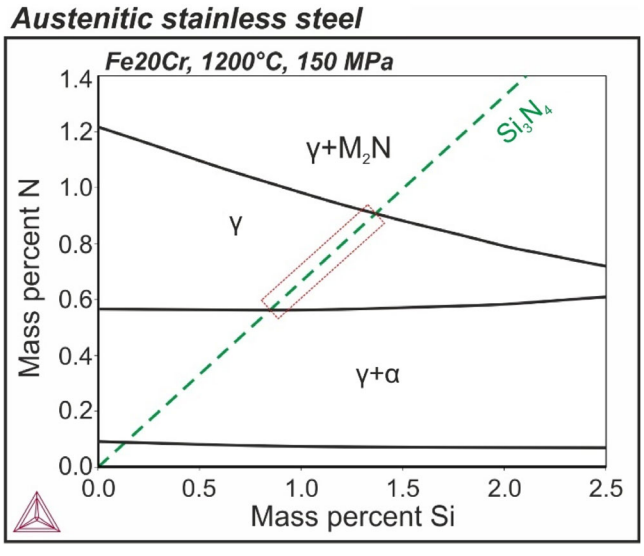

Figure 13. Isothermal phase diagrams calculated using the CALPHAD method at a temperature of 1200 °C and a pressure of 150 MPa for the Fe20Cr systems.

stability or a low tendency for phase transformation during cooling must be ensured. This is accomplished in the present scenario by setting sufficiently high-nitrogen content as well as a chromium content of 20 mass%. The elevated chromium level should lower the temperature at which thermally induced martensitic transformation occurs to below room temperature, thereby ensuring the formation and preservation of a single-phase austenitic structure at room temperature.

The motivation for developing a nickel-free austenitic stainless steel arises from the need to reduce reliance on the expensive and often volatile nickel market. Furthermore, the high abundance of nitrogen (comprising 78% of the atmosphere) and its role in enhancing sustainability are key factors driving the exploration of this alternative austenitic stainless steel production route. In the context of AM, the utilization of this alloy system could unlock new applications, particularly in medical technology, where AM is employed to create patient-specific implants. The absence of nickel is especially significant, as it mitigates the risk of nickel-induced allergic reactions in the human body.

7.2. Duplex Stainless Steels

In addition to producing a single-phase austenitic steel based solely on the FeCr(Si)N system, a duplex stainless steel can also be produced using the process routes outlined in this work (HIP and PBF-LB/M + HIP). As with the austenitic variant, this is driven by the objective of reducing or eliminating the nickel content. The feasibility is evidenced by the CALPHAD calculations shown in **Figure 14**. Figure 14a presents the isothermal phase diagram of the Fe22Cr system at a temperature of 1145 °C and a pressure of 150 MPa, with nitrogen content plotted along the *y*-axis and silicon content along the *x*-axis. The elevated chromium content of 22 mass%, compared to the austenitic steel variant, ensures sufficient stabilization of the ferritic phase at high temperatures, enabling the formation of a two-phase ferritic–austenitic microstructure in the course of solution annealing. With an exemplary nitrogen content of 0.4 mass% (see indicated cross in Figure 14a) and a corresponding silicon content of 0.6 mass%, the addition of Si_3N_4 places the system within the phase region consisting of alpha and gamma iron. The corresponding phase quantity diagram for this composition, shown in Figure 14b, indicates that at a temperature of 1145 °C and a pressure of 150 MPa, a phase mixture consisting of 50 vol% ferrite and 50 vol% austenite can be achieved, corresponding to a typical duplex stainless steel structure. Similar to the preservation of a single-phase austenitic structure, this phase mixture can be maintained down to room temperature through HIP-internal gas quenching, thereby enabling the production of duplex stainless steel via Si_3N_4 addition in the HIP.

7.3. Martensitic Stainless Steel

As described in Section 1 and 2, the strength attainable in carbon-alloyed martensitic stainless steels is primarily dictated by the carbon content and the resulting degree of tetragonal lattice distortion during or after hardening. However, alloying with carbon is constrained by the increasing risk of forming Cr-rich $M_{23}C_6$ carbides, which can significantly compromise corrosion resistance by depleting chromium from the matrix. An alternative to carbon is the alloying element nitrogen, which induces martensitic transformation and also offers positive effects on corrosion resistance, including increased resistance to pitting corrosion (see Equation (1)). However, due to the limited solubility of nitrogen in the melt, producing such steels is challenging. The approach described in the present work, which allows for the incorporation of high-nitrogen contents, makes production feasible in principle. The isothermal phase diagram of the Fe15Cr system, calculated at a temperature of 1200 °C and a pressure of 150 MPa, as shown in **Figure 15**, serves as an illustration of the feasibility. As shown in the isothermal phase diagrams in Figure 13 and 14a, the nitrogen content is plotted against the silicon content. An example marker has been placed at a nitrogen content of 0.6 mass% with a corresponding silicon content of 0.9 mass%, which is adjusted by Si_3N_4 addition. While a chromium content of 20 mass% was selected for the austenitic steel to prevent martensitic transformation during cooling (see Figure 13), a deliberately lower chromium content is considered for the martensitic stainless steel in Figure 15 to induce

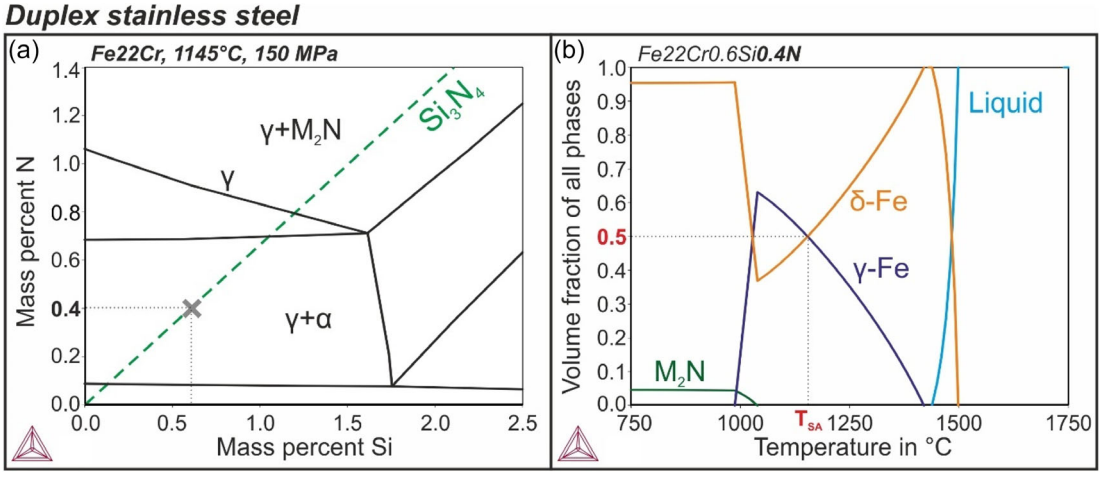

Figure 14. a) Isothermal phase diagrams calculated using the CALPHAD method at a temperature of 1145 °C and a pressure of 150 MPa for the Fe22Cr systems. b) Phase quantity diagram of Fe20Cr0.6Si0.4N as a function of temperature (T_{SA} = Solution annealing temperature).

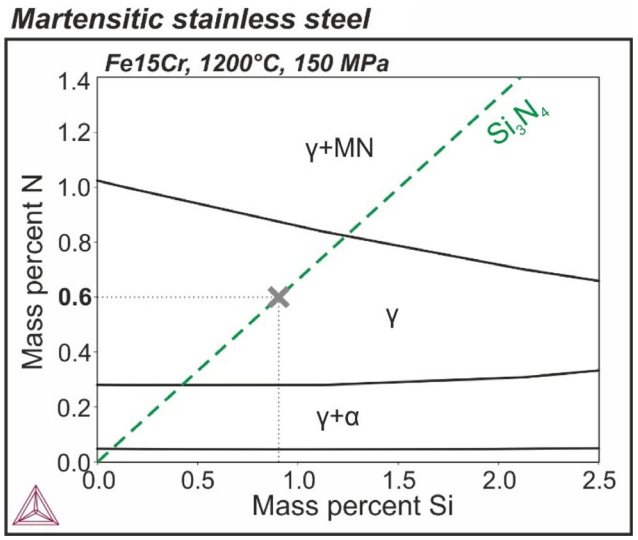

Figure 15. Isothermal phase diagrams calculated using the CALPHAD method at a temperature of 1200 °C and a pressure of 150 MPa for the Fe15Cr systems.

martensitic transformation during HIP-internal gas quenching. Such a steel would represent a significant innovation, particularly in the field of AM. Studies on PBF-LB/M manufacturing of nitrogen-alloyed martensitic stainless steels, such as X30CrMoN15-1 (Cronidur 30, 1.4108), have demonstrated that due to the limited nitrogen solubility in the melt, an N content of only 0.14 mass% can be achieved.[53] Consequently, the corrosion resistance and mechanical properties typically associated with the standard composition of this steel (nitrogen content of 0.3–0.5 mass%) cannot be fully realized until now.

7.4. Additional Overall Research Question

While previous investigations on CrNi steels have consistently resulted in a single-phase austenitic structure, the application of the Si_3N_4 addition approach to other steel groups could yield different outcomes. The observed opposing segregation behaviors of silicon and nitrogen, along with the resulting variations in local austenite stability, suggest that the formation of ferrite fractions during HIP is theoretically possible. This outcome would be desirable in the case of duplex steels but would be detrimental to achieving a single-phase austenitic or martensitic steel. Therefore, future research must focus on understanding the dissolution behavior of Si_3N_4 during HIP in different FeCr systems, particularly in relation to the interaction between chemical heterogeneity and phase formation mechanisms.

Acknowledgements

The authors kindly acknowledge the financial support of the German Research Foundation (DFG) within the project 493947509 "Influence of an Si_3N_4 powder additive on the PBF-LB processability of stainless steels and the microstructure development during PBF-LB and subsequent HIP-URQ redensification," which is part of the priority program SPP2122 "Materials for Additive Manufacturing (MATframe)."

Open Access funding enabled and organized by Projekt DEAL.

Conflict of Interest

The authors declare no conflict of interest.

Author Contributions

Louis Becker: Conceptualization (lead); Data curation (lead); Formal analysis (lead); Investigation (lead); Methodology (lead); Validation (lead); Visualization (lead); Writing—original draft (lead); Writing—review & editing (equal). **Felix Radtke**: Conceptualization (supporting); Data curation (equal); Formal analysis (supporting); Investigation (supporting); Validation (supporting); Visualization (supporting); Writing—original draft (supporting); Writing—review & editing (equal). **Jonathan Lentz**: Conceptualization (equal); Methodology (equal); Project administration (equal); Supervision (equal); Writing—review & editing (equal). **Simone Herzog**: Conceptualization (supporting); Methodology (supporting); Project administration (equal); Supervision (equal); Writing—review & editing (supporting). **Christoph Broeckmann**: Funding acquisition (lead); Resources (lead); Supervision (equal); Writing—review & editing (supporting). **Sebastian Weber**: Conceptualization (equal); Funding acquisition (lead); Resources (lead); Supervision (lead); Writing—review & editing (supporting).

Keywords

additive manufacturing, diffusion alloying, high-nitrogen stainless steels, powder metallurgy

Received: August 30, 2024
Revised: October 16, 2024
Published online:

[1] A. Di Schino, *Manufacturing and Application of Stainless Steels*, MDPI - Multidisciplinary Digital Publishing Institute, Switzerland **2020**.
[2] J. Ki Leuk Lai, K. Ho Lo, C. Hung Shek, *Stainless Steels: An Introduction and their Recent Developments*, Bentham Science Publishers **2012**.
[3] H. Berns, W. Theisen, *Ferrous Materials: Steel and Cast Iron*, Springer Berlin/Heidelberg, Berlin, Heidelberg **2008**.
[4] *Prevention, Diagnosis, Repair, Second., Completely Rev. and Enlarged Ed.*, Wiley-VCH, Weinheim **2013**.
[5] A. J. Sedriks, *Corrosion of Stainless Steels*, 2nd ed., Wiley, New York, NY **1996**.
[6] *Systematische Beurteilung Technischer Schadensfälle* (Eds: G. Lange, M. Pohl), Wiley-VCH, Weinheim, Germany **2014**.
[7] M. Speidel, in *Ultra High Strength Austenitic Stainless Steels, Stainless Steels World Conf. Proc.*, Den Haag, November **2001**, pp. 98–106.
[8] I. Varol, J. C. Lippold, W. A. Baeslack, *Key Eng. Mater.* **1992**, *69–70*, 217.
[9] W. Gordon, A. van Bennekom, *Mater. Sci. Technol.* **1996**, *12*, 126.
[10] M. Amuda, S. Mridha, *Adv. Mater. Res.* **2009**, *83–86*, 1165.
[11] E. G. Ellison, A. Al-Zamily, *Fatigue Fract. Eng. Mater. Struct.* **1994**, *17*, 39.
[12] H. Berns, V. Gavriljuk, S. Riedner, *High Interstitial Stainless Austenitic Steels*, Springer Berlin Heidelberg, Berlin, Heidelberg **2013**.
[13] K. Lefor, M. Walter, A. Weddeling, E. Hryha, S. Huth, S. Weber, L. Nyborg, W. Theisen, *Metall. Mater. Trans. A* **2015**, *46*, 1154.
[14] *Microstructure, Properties and Applications*, Abington Publishing, Cambridge, England **1997**.
[15] I. Alvarez-Armas, S. Degallaix-Moreuil, *Duplex Stainless Steels*, J. Wiley, London, Hoboken, NJ **2009**.
[16] R. N. Gunn, *Microstructure, Properties and Applications*, Abington Publishing, Cambridge, England **1997**.

[17] A. M. Kumar, I.-H. Toor, *Mater. Corros.* **2022**, *73*, 1687.
[18] F. M. Abdallah, I.-H. Toor, *Arabian J. Sci. Eng.* **2020**, *45*, 599.
[19] V. G. Gavriljuk, H. Berns, *Structure, Properties, Manufacture, Applications*, Springer, Berlin, Heidelberg **1999**.
[20] H. Zitter, L. Habel, *Arch. Eisenhüttenwes.* **1973**, *44*, 181.
[21] Y. Wang, Z. Wang, W. Wang, B. Ma, *Mater. Sci. Eng., A* **2023**, *884*, 145549.
[22] B. D. Shanina, V. G. Gavriljuk, H. Berns, F. Schmalt, *Steel Res.* **2002**, *73*, 105.
[23] V. G. Gavriljuk, S. P. Efimenko, Y. E. Smuk, S. Y. Smuk, B. D. Shanina, N. P. Baran, V. M. Maksimenko, *Phys. Rev. B* **1993**, *48*, 3224.
[24] S. C. Krishna, N. K. Karthick, A. K. Jha, B. Pant, P. V. Venkitakrishnan, *Metall. Microstruct. Anal.* **2017**, *6*, 425.
[25] S. Liu, X. Wu, L. Shi, Y. Wu, W. Qu, *J. Mater. Sci. Chem. Eng.* **2015**, *3*, 37.
[26] Z. Jiang, H. Li, Z. Chen, Z. Huang, D. Zou, L. Liang, *Steel Res. Int.* **2005**, *76*, 740.
[27] J. W. Simmons, *Mater. Sci. Eng., A* **1996**, *207*, 159.
[28] Nichtrostende Stähle – Teil 1: Verzeichnis der nichtrostenden Stähle; Deutsche Fassung EN 10088-1:2014, **2014**.
[29] A. Sieverts, *Z. Phys. Chem.* **1931**, *155A*, 299.
[30] *Nitrogen-Alloyed Austenitic Stainless Steels and their Properties* **1993**.
[31] H.-B. Li, Z.-H. Jiang, Y. Cao, Z. Zhang, *Int. J. Miner. Metall. Mater.* **2009**, *16*, 387.
[32] A. Mitchell, H. Frederiksson, *J. Mater. Sci.* **2004**, *39*, 7275.
[33] J. C. Rawers, N. A. Gokcen, R. D. Pehlke, *Metall. Trans. A* **1993**, *24*, 73.
[34] J. Yu, F. Liu, Z. Jiang, H. Li, C. Kang, W. Zhang, A. Wang, X. Geng, *ISIJ Int.* **2020**, *60*, 1684.
[35] L. Becker, F. Radtke, J. Lentz, S. Herzog, C. Broeckmann, S. Weber, *Mater. Lett.* **2023**, *352*, 135119.
[36] J. Rösler, H. Harders, M. Bäker, *Mechanisches Verhalten der Werkstoffe*, 6th aktualisierte Auflage, Springer Vieweg, Wiesbaden **2019**.
[37] H. Mughrabi, *HTM J. Heat Treat. Mater.* **2001**, *56*, 300.
[38] F. Klubberg, M. Hempen, P. Beiss, in *Vortrags- und Diskussionstagung Werkstoffprüfung 1998*, **1998**, pp. 303–312.
[39] I. Gibson, D. Rosen, B. Stucker, M. Khorasani, *Additive Manufacturing Technologies*, 3rd ed., Springer, Cham, Switzerland **2021**.
[40] J. O. Milewski, *Additive Manufacturing of Metals*, Springer International Publishing, Cham **2017**.
[41] F. Bosio, A. Aversa, M. Lorusso, S. Marola, D. Gianoglio, L. Battezzati, P. Fino, D. Manfredi, M. Lombardi, *Mater. Des.* **2019**, *181*, 107949.
[42] D. Bourell, J. P. Kruth, M. Leu, G. Levy, D. Rosen, A. M. Beese, A. Clare, *CIRP Ann.* **2017**, *66*, 659.
[43] A. Gebhardt, J.-S. Hötter, *Additive Manufacturing: 3D Printing for Prototyping and Manufacturing*, Hanser Publications; Hanser Publishers, Cincinnati, OH; Munich **2016**.
[44] T. DebRoy, H. L. Wei, J. S. Zuback, T. Mukherjee, J. W. Elmer, J. O. Milewski, A. M. Beese, A. Wilson-Heid, A. De, W. Zhang, *Prog. Mater. Sci.* **2018**, *92*, 112.
[45] P. Bajaj, A. Hariharan, A. Kini, P. Kürnsteiner, D. Raabe, E. A. Jägle, *Mater. Sci. Eng., A* **2020**, *772*, 138633.
[46] J. Boes, A. Röttger, L. Becker, W. Theisen, *Addit. Manuf.* **2019**, *30*, 100836.
[47] F. Radtke, L. Becker, S. Herzog, J. Lentz, S. Weber, C. Broeckmann, in *Euro Powder Metallurgy 2023 Congress & Exhibition*, Lisbon, Portugal, October **2023**, https://doi.org/10.59499/EP235764243.
[48] F. Radtke, L. Becker, S. Herzog, J. Lentz, S. Weber, C. Broeckmann, in *LiM 2023 Proc.- Laser Powder Bed Fusion*, Munich, Germany, June **2023**, https://doi.org/10.18154/RWTH-2023-10113.
[49] A. Kaletsch, F. Radtke, S. Herzog, P. Köhnen, S. Höges, C. Broeckmann, *Appl. Sci.* **2023**, *13*, 12676.
[50] T. Spusta, J. Svoboda, K. Maca, *Acta Mater.* **2016**, *115*, 347.
[51] L. Becker, F. Radtke, J. Lentz, S. Herzog, C. Broeckmann, S. Weber, *Manuf. Lett.* **2024**, *9*, 100205.
[52] L. Becker, F. Radtke, J. Lentz, S. Herzog, C. Broeckmann, S. Weber, in *Euro Powder Metallurgy Congress & Exhibition*, Malmo, Sweden, October **2024**, https://doi.org/10.59499/EP246252913.
[53] J. Boes, A. Röttger, W. Theisen, C. Cui, V. Uhlenwinkel, A. Schulz, H.-W. Zoch, F. Stern, J. Tenkamp, F. Walther, *Addit. Manuf.* **2020**, *34*, 101379.